Dark Energy Survey Year 1 Results: Wide-field mass maps via forward fitting in harmonic space

B. Mawdsley [1]★ D. Bacon,[1] C. Chang [2,3] P. Melchior [4] E. Rozo,[5] S. Seitz, [6,7]
N. Jeffrey [8] M. Gatti,[9] E. Gaztanaga [10,11] D. Gruen [12,13,14] W. G. Hartley,[8,15]
B. Hoyle,[6,7] S. Samuroff [16] E. Sheldon,[17] M. A. Troxel,[18] J. Zuntz [19]
T. M. C. Abbott,[20] J. Annis,[21] E. Bertin,[22,23] S. L. Bridle,[24] D. Brooks,[8]
E. Buckley-Geer,[21] D. L. Burke,[13,14] A. Carnero Rosell [25,26] M. Carrasco Kind [27,28]
J. Carretero,[9] L. N. da Costa,[26,29] J. De Vicente,[25] S. Desai,[30] H. T. Diehl,[21]
P. Doel,[8] A. E. Evrard [31,32] B. Flaugher,[21] P. Fosalba,[10,11] J. Frieman,[3,21]
J. García-Bellido,[33] D. W. Gerdes,[31,32] R. A. Gruendl,[27,28] J. Gschwend,[26,29]
G. Gutierrez,[21] D. L. Hollowood,[34] K. Honscheid,[35,36] D. J. James,[37] M. Jarvis,[38]
T. Jeltema,[34] K. Kuehn,[39] N. Kuropatkin,[21] M. Lima,[26,40] M. A. G. Maia,[26,29]
J. L. Marshall,[41] R. Miquel,[9,42] A. A. Plazas [4] A. Roodman,[13,14] E. Sanchez,[25]
V. Scarpine,[21] S. Serrano,[10,11] I. Sevilla-Noarbe,[25] M. Smith [43] R. C. Smith,[20]
F. Sobreira,[26,44] E. Suchyta [45] M. E. C. Swanson,[28] G. Tarle,[32] D. L. Tucker,[21]
V. Vikram,[46] and A. R. Walker[20] (DES Collaboration)

Affiliations are listed at the end of the paper

ABSTRACT
We present new wide-field weak lensing mass maps for the Year 1 Dark Energy Survey (DES) data, generated via a forward fitting approach. This method of producing maps does not impose any prior constraints on the mass distribution to be reconstructed. The technique is found to improve the map reconstruction on the edges of the field compared to the conventional Kaiser–Squires method, which applies a direct inversion on the data; our approach is in good agreement with the previous direct approach in the central regions of the footprint. The mapping technique is assessed and verified with tests on simulations; together with the Kaiser–Squires method, the technique is then applied to data from the DES Year 1 data and the differences between the two methods are compared. We also produce the first DES measurements of the convergence Minkowski functionals and compare them to those measured in simulations.

Key words: gravitational lensing: weak – dark matter – large-scale structure of Universe.

1 INTRODUCTION

The presence of a gravitational potential influences light trajectories so that, to an observer, the apparent position and shape of objects is altered via an effect known as *gravitational lensing*. As this gravitational potential is related to the matter distribution, there is a relationship between the strength of the lensing effect and the density contrast from which it arises. The arrangement of a source of light, a mass distribution acting as a lens, and an observer can produce a range of magnitudes of lensing effects. This paper pertains to weak lensing, which produces small $\lesssim 1$ per cent changes in the source objects' apparent ellipticities. Measurements of galaxy ellipticities can therefore be used to estimate lensing *shear*, and hence constrain the integrated gravitational potential and the integrated matter distribution between the observer and a lensed galaxy. Shear can be related to the matter surface density, or *convergence* distribution κ, through a technique known as the Kaiser–Squires inversion (Kaiser & Squires 1993) to produce large-scale maps.

★ E-mail: ben.mawdsley@port.ac.uk

As the perturbations to the underlying metric of the Universe from matter concentrations are solely caused by gravitation, lensing is only sensitive to the total density contrast and not to any further properties of the matter. Lensing therefore probes the dark Universe as well as luminous matter. This is in marked contrast to using other probes, such as galaxy clustering, where luminous matter is a proxy for the location of dark matter and we must introduce a bias parameter. Lensing, and the matter distributions inferred from it, are powerful tools to constrain cosmological parameters – and this is not just true of the two-point statistics of shear or convergence; the κ maps contain further information on the phase of the matter distribution. Additional non-Gaussian information in the fields has been examined through peak statistics of the convergence field (Dietrich & Hartlap 2010; Kratochvil, Haiman & May 2010; Yang et al. 2011; Kacprzak et al. 2016), Minkowski Functionals (Petri et al. 2013, 2015), three point statistics (Dodelson & Zhang 2005), and through examination of the full distribution of values in the convergence map, or Probability Density Function (Clerkin et al. 2015; Patton et al. 2017). Maps are also useful for cross-correlating with other observations, for example by correlating with galaxy positions (Utsumi et al. 2016) and for constraining bias as in Chang et al. (2016).

With the next generation of surveys covering significant fractions of the sky and measuring large numbers of galaxy shapes to high precision, weak lensing promises to be a leading cosmological probe in coming years, and will map the large-scale structure of the Universe to an unprecedented scale. Wide-field mass maps have been produced using weak lensing measurements in a number of recent surveys: the Canada-France Hawaii Telescope Lensing Survey (Erben et al. 2013), the Cosmic Evolution Survey (Massey et al. 2007), and the Kilo-Degree Survey (de Jong et al. 2015). The Dark Energy Survey (DES; Flaugher 2005) has produced mass maps through the Kaiser–Squires inversion, on an approximately flat-field in their Science Verification data (Vikram et al. 2015) and on the sphere for the larger Year 1 footprint (Chang et al. 2018). The Hyper Suprime-Cam survey (Aihara et al. 2018a,b) has produced mass maps (Miyazaki et al. 2018) using their shear catalogues (Mandelbaum et al. 2018) over a 167 deg^2 area of the sky. Maps were also produced tomographically across several redshift bins (Oguri et al. 2018), resolving structure at a finer level than DES due to its high galaxy density, allowing for smaller scale shear measurements.

In this paper, we produce updated mass maps using the DES Year 1 data. Previously, maps were made through directly transforming shear fields into convergence maps, which introduces errors around the edges of the survey footprint; our alternative method avoids directly transforming data and prevents the introduction of these edge effects, by fitting hypothesis full-sky maps to the data. We examine how this method compares to the previous approach, and analyse its potential for further applications to wide-field mass mapping.

This paper is arranged into five sections. Section 2 describes the weak lensing formalism, before introducing the forward fitting approach in Section 3. Section 4 provides details of the tests undertaken to examine the resultant maps, and Section 5 presents the maps produced using the DES Y1 data. We conclude in Section 6.

2 LENSING FORMALISM

Here we briefly describe the relevant weak lensing formalism for our work. A comprehensive review of weak lensing can be found in Bartelmann & Schneider (2001); in the following Section we

shall follow the spherical harmonics approach described in Castro, Heavens & Kitching (2005). The large footprint of modern surveys mean that a full sky treatment is required, which is achieved with techniques commonly used in CMB analyses (Heavens 2003; Kitching et al. 2014; Leistedt et al. 2017)

We can define a *lensing potential* ϕ at a given spatial coordinate $\boldsymbol{r} = (r, \theta, \psi)$ by

$$\phi(r, \theta, \psi) = \frac{2}{c^2} \int_0^r \mathrm{d}r' \frac{f_K(r - r')}{f_K(r) f_K(r')} \Phi(r', \theta, \psi), \tag{1}$$

where Φ is the Newtonian potential and f_k is a comoving angular diameter distance, taking values of ($\sin r$, r, or $\sinh r$) for a Universe with curvature described by $k = 1$ (closed), 0 (flat), or -1 (open), (Castro et al. 2005). The coordinate r is a radial distance and (θ, ϕ) refer to angular positions on the sky. This potential can be related to the matter density through Poisson's equation

$$\nabla_r^2 \Phi(\boldsymbol{r}) = \frac{3\Omega_m H_0^2}{2a(t)} \delta(\boldsymbol{r}), \tag{2}$$

where Ω_m is the present day total matter density parameter, H_0 is the Hubble constant at the present time, $a(t)$ is the scale factor, and $\delta(\boldsymbol{r})$ is the density contrast at position $\boldsymbol{r}$.

We shall consider the case of a scalar field $\phi(\boldsymbol{r})$ in a flat background geometry, which can be transformed into the basis of spherical harmonics and spherical Bessel functions via

$$\phi_{\ell m}(k) = \sqrt{\frac{2}{\pi}} \int \mathrm{d}^3 r \phi(\boldsymbol{r}) k j_\ell(kr) Y_{\ell m}^*(\theta, \varphi). \tag{3}$$

Through the introduction of a geometrical differential operator $\eth(\bar{\eth})$, which raises (lowers) the spin of the field, ψ can be related to the shear γ and convergence κ through the following relations:

$$\kappa(\boldsymbol{r}) = \frac{1}{4}(\eth\bar{\eth} + \bar{\eth}\eth)\phi(\boldsymbol{r}), \tag{4}$$

$$\gamma(\boldsymbol{r}) = \frac{1}{2}\eth\eth\phi(\boldsymbol{r}), \tag{5}$$

where $\gamma(\boldsymbol{r})$ is composed of two orthogonal components

$$\gamma_1(\boldsymbol{r}) = \frac{1}{4}(\eth\eth + \bar{\eth}\bar{\eth})\phi(\boldsymbol{r})$$

$$\gamma_2(\boldsymbol{r}) = -\frac{i}{4}(\eth\eth - \bar{\eth}\bar{\eth})\phi(\boldsymbol{r}). \tag{6}$$

Furthermore, as shear is a spin-2 field, it will decompose into spin-2 weight spherical harmonics ($_2\gamma_{\ell m}$), known as E and B modes, that are free of curl and divergence, respectively. In the single thin lens plane case, it can be shown that the lensing information is contained within the E mode coefficients (Castro et al. 2005), and that the B mode coefficients should only be non-zero in the presence of noise. Multiple lenses can give rise to a small B mode, but these will be negligible given our signal-to-noise. Because of the $\eth$ operator rules for spherical harmonics, the equations relating coefficients for ϕ, κ, γ, and lensing deflection α are:

$$_2\gamma_{\ell m}(k) = -A_{E,\ell m} = \frac{1}{2}\sqrt{\frac{(\ell+2)!}{(\ell-2)!}}\phi_{\ell m}(k), \tag{7}$$

$$\kappa_{\ell m}(k) = -\frac{\ell(\ell+1)}{2}\phi_{\ell m}(k), \tag{8}$$

$$\alpha_{\ell m} = \sqrt{\ell(\ell+1)}\phi_{\ell m}(k), \tag{9}$$

where $\phi_{\ell m}(k)$ are the coefficients of the lensing potential in spherical harmonics. Using these quantities in harmonic space, we can transform an observed sky shear signal to maps of the quantities κ, α, and ϕ.
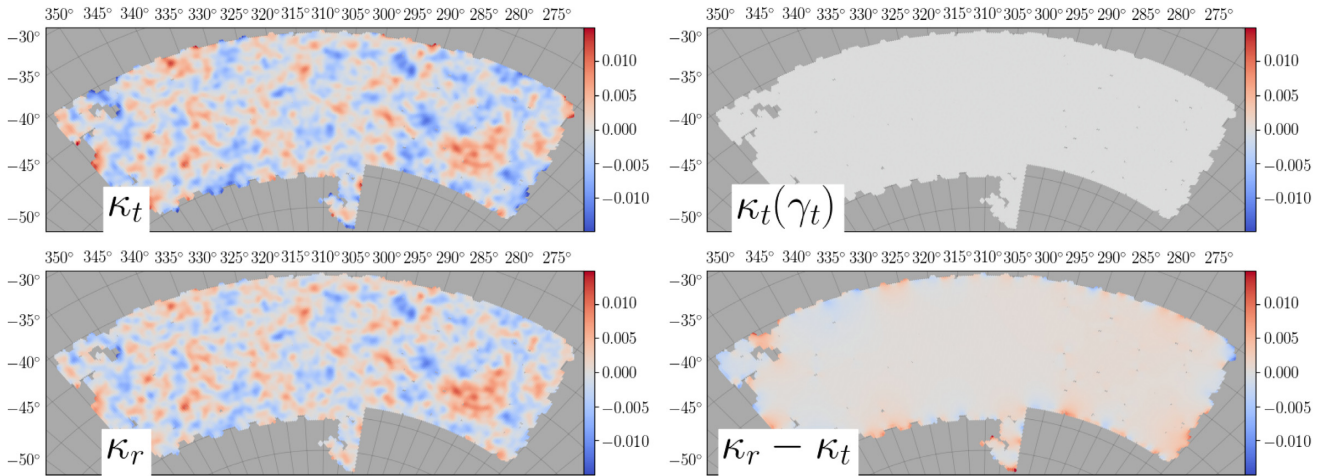
Figure 1. Comparison of reconstructions performed using κ_t, γ_1, and γ_2 on maps of nside = 256, using the Kaiser Squires direct inversion technique. These pixels have a width of ~0.23 deg and the maps are smoothed with a Gaussian kernel with $\sigma = 20$ deg. Upper left shows a true κ distribution, and upper right shows the residuals for a reconstruction of this field when using the full sky of γ_1 and γ_2 values, without shape noise added. Lower left shows the reconstruction of the map using shear values from only the survey region, and the lower right the residuals for this approach. Comparing the two right hand plots shows clearly that considerable residuals can arise in the edge pixels of the survey footprint, even before the addition of shape noise, and the scale of this error can be of a similar size to the κ field that we are attempting to reconstruct.

Shear is estimated using galaxy ellipticities ϵ; by averaging over a significant number of galaxies and in the absence of intrinsic alignments, ellipticities not due to lensing should average to give a (noisy) mean ellipticity of zero; any remaining signal is due to the lensing shear γ, i.e

$$\epsilon = \gamma + \epsilon_{\rm int} + \epsilon_s, \qquad (10)$$

where ϵ_s is the noise associated with estimating a galaxy shape, $\epsilon_{\rm int}$ is the intrinsic shape of the galaxy, and ϵ is the observed distortion. Averaging this estimator for a large number of galaxies will reduce the noise, so it is desirable to have the densest possible background field of lensed galaxies.

3 METHODOLOGY

There are two methods used in this paper – the Kaiser–Squires reconstruction applied directly to the data, and our forward-fitting method utilizing hypothesized full-sky shear fields. Both are expressed in spherical harmonics, and use the same γ to κ pipeline. However, they do differ through the shear fields used, as the forward fitting model uses hypothesis full-sky shear fields, while the direct inversion uses shear data from the survey footprint.

In order to produce maps on the scales covered by DES Y1, a package that utilizes the spherical approach is needed. We use the HEALPY suite which is a python wrapper for HEALPIX,[1] software which is designed to handle data on the sphere and initially developed for use with the cosmic microwave background. The spin-2 γ observations are analogous to the polarization Stokes parameters Q and U. Estimated maps of γ_1 and γ_2 are entered as arguments in the function MAP2ALM to produce their spherical harmonics coefficients in the form of the divergence free $B_{\ell m}$ and the curl free $E_{\ell m}$.

3.1 Direct inversion

Kaiser–Squires on the sphere uses the E modes found from a spherical transform of a shear field with equation (7) to produce

convergence coefficients; the B mode coefficients $B_{\ell m}$ serve as a useful null test for possible systematics and noise. Final maps are produced via the reverse transform ALM2MAP, with κ and ϕ using the spin-0 case of the transform and α the spin-1 case (equations 8 and 9). The output is a HEALPY map, pixelized to a chosen resolution, and then smoothed using the Smoothing function. Producing maps at a higher resolution reduces the magnitude of the edge effects, and smoothing improves the signal to noise. All maps in this paper are displayed using the Albers Equal Area projection and using SKYMAPPER.[2]

Fig. 1 shows simulated skies reconstructed with the direct inversion. Using a full sky of known γ (right top), the reconstruction from γ to κ has negligible residuals. However, when an area of limited shear data is used, the reconstruction introduces significant errors along the edges of the data footprint (right bottom). These arise due to the assumption that the complete field is sampled, when in reality it is not; unobserved regions of the sky are treated as having zero shear and some bias in the true harmonic coefficients is introduced. These errors are significant fractions of the typical κ values, which is apparent when comparing the size of residuals in Fig. 1 to the true κ field. This can result in significant contamination of the recovered map. In this paper, we will refer to making maps this way, from a finite survey area, as the *direct inversion* method.

3.2 Forward fitting approach

We have developed a forward fitting approach with the aim of mitigating some of the limitations of the direct inversion. The direct inversion method was initially developed with two assumptions – that the field is uniform in its noise, and that the shear field is completely observed. Creating mass maps with a field that has been observed over a fraction of the sky and with a non-uniform noise distribution will violate these assumptions and therefore introduce errors in the reconstructed map (Seitz & Schneider 1995, 2001). The

---

[1]http://healpix.sf.net/
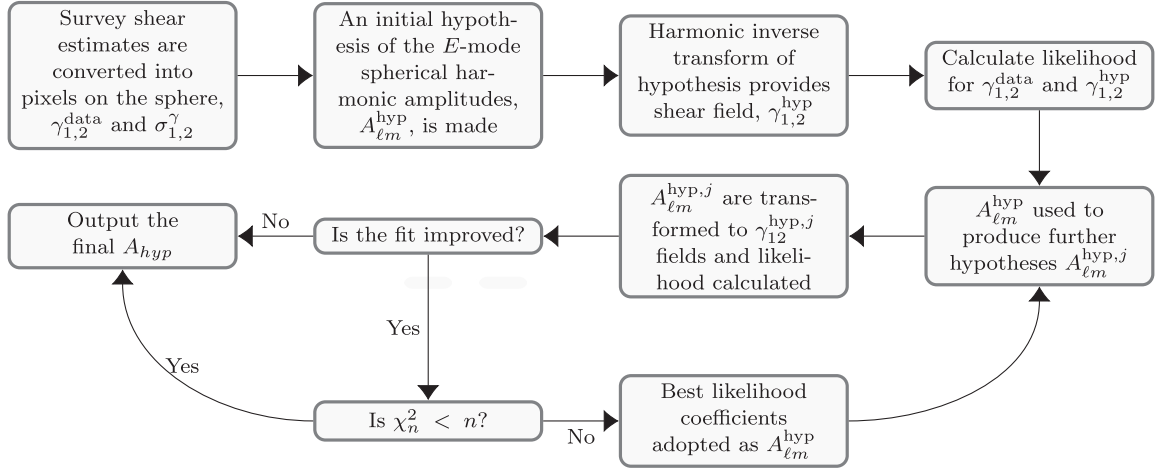
[2]https://github.com/pmelchior/skymapper

Figure 2. Graphical representation of the forward fitting routine, describing the iterative nature of the process. Hypotheses are produced in the harmonic space and compared to the data in real space, gradually increasing the likelihood through subsequent selection of improved hypotheses. B modes are set to zero, and only E modes are hypothesized.

motivation for the forward-fitting technique is therefore to produce maps using the usual relationship between γ and κ fields, but to do so in such a way that they are made without transforming the limited shear measurements directly into spherical harmonics.

Our technique instead hypothesizes a full sky of shear values, and then compares this hypothesis to the observations. Thus, the masked data do not directly enter the transform and the edge effects introduced by the direct inversion are avoided. Comparing a region of the hypothesized sky γ values to the observed γ, with well estimated errors, allows these realizations to become constrained by the data.

The method was written in python and made use of the packages HEALPY and NUMPY.[3] The whole procedure is shown graphically in Fig. 2, and described below:

(i) An initial shear hypothesis, $A_{\ell m}^{\mathrm{hyp}}$, is made for the E modes in harmonic space (up to an ℓ of 2 nside -1), and transformed to give its corresponding full sky shear fields γ through use of the HEALPY function ALM2MAP. We choose to make our initial hypothesis through generating an E mode harmonic corresponding to a Gaussian random sky with variance typical of the observed galaxy overdensity field. We do not use the actual overdensity field to inform this initial hypothesis, beyond using it as an estimate of the size of fluctuations in the field. This initial guess is far from the minimum, but early iterations from this guess take large steps down the likelihood surface.

(ii) The hypothesized shear field is compared to observed data on the sphere γ_{obs} with known errors σ_γ by calculating its likelihood. The quantity σ_γ is an estimate of the error on the shear measurement in a pixel, and is found by taking the standard error on the mean, using the galaxy shape measurements in that pixel. Assuming Gaussian errors and independent measurements, the log-likelihood is proportional to

$$\chi^2 = \sum_{i \in \mathrm{footprint_{pix}}} \frac{(\gamma_{\mathrm{hyp},i} - \gamma_{\mathrm{obs},i})^2}{\sigma_{\gamma,i}^2}, \tag{11}$$

where footprint$_{\mathrm{pix}}$ is the set of pixels contained in the survey footprint. We find that the diagonal terms of the covariance are dom-

inant, and a full pixel-by-pixel covariance matrix is prohibitively computationally expensive. As we will be using maps of an *nside* = 256 in this paper, we tested the reliability of assuming a diagonal covariance matrix by using maps at this resolution with 600 galaxies in a pixel, mimicking the Buzzard footprint that will be more fully introduced in Section 4.3. When we investigated the covariance of a pixel with its neighbour across simulated maps, we found that the covariance with respect to the immediately neighbouring pixel is at a value approximately 4.5 per cent of the variance within the pixel; the corresponding inverse covariance matrix is well approximated as diagonal with elements equal to the reciprocal of the variance. This off-diagonal contribution to the covariance matrix comes from the cosmic shear signal, where large-scale structure introduces coherent distortions across the sky. The amplitude of the off-diagonal contributions is therefore dependent upon the cosmology and resolution of the map. Further, we wish to identify a confidence region for convergence pixel values; since equation (11) follows a χ_n^2 distribution where n is the number of pixels, and we are fitting n parameters (i.e. pixel values), the 68 per cent confidence region is bounded by $\chi^2/n \simeq 1$.

(iii) $A_{\ell m}^{\mathrm{hyp}}$ serves as the basis for a series of similar E mode harmonics, A_{lm}^j, produced through randomly perturbing the coefficients of the m modes of a particular randomly chosen ℓ, by adding a contribution to each m drawn randomly from a Gaussian with standard deviation (s.d) determined by the power in the current best hypothesis at that ℓ mode. We choose to produce 10 perturbed hypotheses, each differing from each other by altering the coefficients at a single ℓ mode.

(iv) Each of these altered hypotheses A_{lm}^j are transformed to produce shear maps γ^j which are then compared to the data and the corresponding likelihood calculated.

(v) The hypothesis with the greatest likelihood is adopted as the new $A_{\ell m}^{\mathrm{hyp}}$ for the next iteration of the routine.

(vi) The cycle repeats until consistency with the data is found ($\chi^2/n < 1$), or a plateau reached from which no improvements to the fit are made after a threshold number of attempts. For the results in this paper, we chose 500 generations without improvement as the exit condition. In practice no runs required this exit condition.

The final A_{lm} can be used directly as E_{lm} in equations (8) and (9) to produce a convergence map. Repeated runs of the fitting

[3]https://docs.scipy.org/doc/

algorithm produce a sampling of the maps consistent with the data. We produce a final map from the average of 40 fitted maps; we will show in later tests that this map provides an unbiased reconstruction of the mass distribution, and assess the errors associated with it in Appendix A.

We can carry out a full sampling of the likelihood using the Metropolis–Hastings MCMC algorithm (Metropolis et al. 1953; Hastings 1970), which we have tested for one of our `synfast` all sky simulations (see Section 4.1), with 10 walkers starting from randomly generated starting points and each storing a sample every 100 steps. We let these walkers run for $\sim 10^6$ steps and all reached $\chi^2/n \simeq 1$, but few outputted maps were at a χ^2 value much lower than this. As we have a high number of pixels, the volume of possible solutions rapidly decreases as χ^2 is lowered and subsequent steps in the direction of an increased likelihood fit become less and less probable. Due to the 786 432 convergence values stored for a full sky map at `nside = 256`, this approach requires Terabytes of storage, which is prohibitive if used for many simulations, as for instance needed in Appendix A. Our approach, averaging only 40 final outcomes of χ^2 descent, allows us to find a point consistent with the mean found from MCMC in an efficient fashion; the mean difference in a pixel between the MCMC output and our approach is $\simeq 0.24\sigma$, (where σ is the standard deviation of κ pixels found in the MCMC run) and there is a Pearson correlation coefficient of 0.92 between the maps made with each method. In addition, we note that via MCMC or direct descent, the maximum-likelihood solution takes a prohibitive time to reach; we do not require this solution as our average reconstruction is fully consistent with the true field (see Section 4.1).

The runtime of the routine is predominantly affected by two variables – the size of the perturbations given to the coefficients and the `nside` resolution of the field being fitted. To optimize the fitting time, we need to minimize the number of steps taken to maximize the likelihood. We find that our routine can perform $\simeq 20\,000$ generations of 10 hypothesis fields at an `nside = 256` and return an output map in $\simeq 24$ h, using 8 cores on the SCIAMA HPC cluster. The direct inversion is much quicker, taking a maximum of 1 min for a field of the same resolution. Due to the nature of the fitting routine, the direct inversion will always be significantly quicker than the forward fit.

Note that other techniques exist using forward fitting, some with more constraining priors. For example, Jeffrey et al. (2018) used DES data with Gaussian and sparsity priors to examine how these affected the reconstructions, and found both to improve on the maps made by the direct inversion. Alsing, Heavens & Jaffe (2017) have used Bayesian Hierarchical Models to simultaneously infer cosmological parameters, power spectrum, and shear maps for CFHTLenS. This sophisticated approach will be very promising for curved sky maps in the future; our method can be considered to be a step towards this approach for wide areas, focusing on the map-making element only.

3.3 Examining the reconstructions

3.3.1 F statistics

There are several statistics that we will use to quantify the success of reconstructions, the first of which are:

$$F_1 = \sqrt{\frac{\langle \kappa_{\mathrm{rec}}^2 \rangle}{\langle \kappa_t^2 \rangle}}; \quad F_2 = \frac{\langle \kappa_t \kappa_{\mathrm{rec}} \rangle}{\langle \kappa_t^2 \rangle}. \tag{12}$$

F_1 measures the consistency with which the amplitude information of the maps is preserved, whereas F_2 is sensitive to how well

phase information is recovered. A result of unity for both statistics would mean that the reconstruction is managing to perfectly capture both the phase and amplitude information in the map,. Once the behaviour of our fields' F_1 is understood, we may be able to account for any changes in amplitude by applying a corrective multiplicative factor across the map, but if F_2 is significantly degraded then this indicates that phase information is lost in the final result. Therefore, we want F_2 to be as high quality as possible, and F_1 to be well understood.

Furthermore, when we measure these statistics in maps including shape noise, it becomes important to correct for the effect of this noise contribution, which we call 'denoising' of the statistics. Consider a reconstructed κ map, composed of two parts:

$$\kappa_{\mathrm{rec}} = \alpha \kappa_{\mathrm{sig}} + \kappa_n, \tag{13}$$

where κ_{sig} is the reconstruction of the true convergence from the true shear, and the κ_n term encapsulates all other noise effects that alter the convergence from its true value, such as edge effects and noise in the measurement of the shear in pixels. If we can successfully model the noise on the κ maps, then we can correct for this noise in F_1; our denoised F_1 therefore becomes

$$F_1 = \sqrt{F_{1,N}^2 - F_{1,n}^2}, \tag{14}$$

where $F_{1,n}$ is the statistic found when producing a map that consists solely of noise, and $F_{1,N}$ is the statistic found from the initial noisy data. Construction of a field consisting solely of noise depends upon the mass reconstruction method being examined due to the different residuals introduced in each approach. We will describe the methodology to achieve this in Section 4.2. We assume that there is no correlation between the convergence κ and the noise in that pixel. The denoising procedure serves as an important test of how well we can model the noise across the map, which is of particular importance when we later attempt to reconstruct moments of the true κ distribution. A denoising procedure that recovers F_1 statistics close to unity indicates that both the reconstruction and the noise are behaving as expected. The F_2 statistic does not require any denoising, under the assumption of no correlation between κ_{true} and the noise contribution. However, introducing multiplicative systematics into the maps (i.e. α in equation 13) will change the F_2 statistic.

3.3.2 Minkowski functionals

Another set of statistics of interest are the Minkowski Functionals, which encode the topological information of a map (Mecke, Buchert & Wagner 1994) and are therefore useful to constrain cosmological models (Kerscher, Schmalzing & Buchert 1996; Schmalzing, Kerscher & Buchert 1996; Petri et al. 2015). Following the notation of Hikage, Komatsu & Matsubara (2006) and Munshi et al. (2012), the three Minkowski Functionals (V_0, V_1, V_2) for a 2D surface are defined as

$$V_0 = \int_{\Sigma} \mathrm{d}a,$$
$$V_1 = \frac{1}{4} \int_{\partial \Sigma} \mathrm{d}l,$$
$$V_2 = \frac{1}{2\pi} \int_{\partial \Sigma} K \mathrm{d}l,$$

and represent integrals across the total area, length, and curvature characteristic of a given excursion set of the map, respectively. We calculate these quantities through the use of angular derivatives on

the sky (Schmalzing & Górski [1997](#)), using the formulae listed in Appendix A of Hikage et al. ([2006](#)). Each are normalized by the area of the complete map. We estimate derivatives through finite differences between neighbouring pixels in a similar way to Petri et al. ([2015](#)) but implemented on the spherical pixel scheme used in these maps. Appendix B gives details of the formulae used to calculate the functionals from a given HEALPIX map.

3.3.3 Pearson correlation

Finally, we will also use the Pearson Correlation coefficient defined as

$$\rho_{X,Y} = \frac{(X - \hat{X})(Y - \hat{Y})}{\sigma_x \sigma_y}. \tag{15}$$

For a perfect correlation of X and Y fields, this will be exactly unity, and deviations from this value provide a measure of the level to which noise can dominate the signal. This statistic does not need a denoising approach. In our analysis, we will be using a reconstructed field and a true κ field as X and Y.

4 SIMULATIONS AND INITIAL TESTS

In this Section we will use simulations of observed γ fields with known κ fields to compare the two reconstruction methods, using the metrics introduced in Section 3.3. In all further maps in this paper, results are for final fitted maps of nside = 256, with a pixel separation of 0.22 deg unless otherwise stated. We use a maximum ℓ mode of 2 nside $- 1 = 511$, for sufficient resolution and speed. Maps are then smoothed with a Gaussian with standard deviation of 20 arcmin. We find that the forward fitting routine consistently performs better than the direct inversion, across a variety of metrics used in this Section. Chang et al. ([2018](#)) produced maps to a resolution of nside = 1024, and results found here are not necessarily directly comparable due to the different resolutions.

4.1 Gaussian map tests

The precision and accuracy of each reconstruction technique needs to be carefully assessed, for both the forward fitting approach and for the direct inversion. There are two main effects that will immediately degrade the reconstruction: the limited survey footprint, and the fact that we observe a shear estimate using a varying number of galaxy ellipticities, which introduces a pixel-by-pixel variation in the noise properties.

To examine these effects, we produced a series of full sky shear and convergence maps using the HEALPY routine synfast. This routine produces Gaussian random fields from an input power spectrum, which for these tests was that of a flat ΛCDM Universe characterized by the parameters $\Omega_m = 0.3$, $\Omega_b = 0.047$, $h = 0.7$, $\sigma_8 = 0.82$, $w = -1$. The power spectrum was calculated using COSMOSIS (Zuntz et al. [2015](#)) which utilizes the camb code (Lewis & Bridle [2002](#)). A 'true' sky convergence distribution is given by the output of synfast, with matching true shears. We fit to 25 different true skies with different noise fields, drawn from the same map of pixel uncertainties matching those of the leading DES simulation effort, the Buzzard simulations, which are described more thoroughly in Section 4.3. For a fairer comparison with our other simulation tests, these uncertainties are calculated for a shear field with an error on γ components of ≈ 0.27 and galaxy number in each pixel obtained from the Buzzard catalogue (mean pixel galaxy count of ≈ 600).

The forward fitting approach was applied to this simulated data and produced converged fits. Maps were also made by the direct inversion, in order to compare the two approaches.

4.1.1 Fidelity metrics

Fig. [3](#) shows how the F statistics behave for these simulations, with the filled region showing the Gaussian field 1-σ spread of results when these are evaluated across the 25 maps. The F_1 statistic has been denoised in this plot and is found to be consistent with 1; this implies that our method of modelling noise is consistent with the true noise within that pixel. For the Kaiser–Squires technique applied to the data, the large errors in outer pixels cause more scatter in the denoised statistic.

Considering the F_2 statistic, we see the direct inversion clearly differs from unity, with the reconstruction becoming worse nearer to the edges. By contrast, the forward fitted map consistently preserves the phase information significantly better across the survey area. This can also be seen in the Pearson correlation coefficient in Fig. [4](#), where the edge effects mean that the coefficient for the direct inversion is ≈ 0.1 lower than our method when evaluated over the 22 830 pixels in the footprint.

4.2 Quantifying noise

The Gaussian maps just introduced in Section 4.1 were also used to estimate the uncertainties on each pixel of the final fitted convergence maps. Appendix A describes our examination of the noise properties of the final fitted maps.

In order to estimate the error in any given pixel, we simulate many Gaussian maps and take the difference between the fitted maps and a known truth. Many such difference maps give a sampling of the error distribution in each pixel, with the standard deviation of residuals in a pixel across these mock maps used as the pixel uncertainty estimate. These simulations use the appropriate shear errors in each pixel for the data we are attempting to simulate. We use 25 simulations of noisy skies to produce our errors. This approach was used to calculate errors for all simulation tests and on the Y1 data. The exact footprint used differs for each application as it is designed to mimic the observational properties of the field being simulated, such as galaxy density and sky coverage, but the methodology involves the same techniques across each use. In this paper, error refers to the standard deviation of the residuals found in this way, and noise refers to a single map realization with values drawn from this distribution for each pixel. All error fields are produced in this fashion unless stated otherwise, including for the denoising procedures of later statistics. An estimate of the noise in a pixel can therefore be produced by sampling from a Gaussian with a standard deviation (s.d) corresponding to the error in a pixel. Full maps can be made by sampling in every pixel of the map, and then smoothing to a desired scale. More typically in this paper, unless specified that more maps are required, we use the residual maps themselves as estimated noise fields for the unknown true κ map, to preserve the correlation between neighbouring pixels. For the direct inversion approach, noise fields are produced by creating shear maps consisting of only shape noise and producing mass maps. Repeating the process many times and taking the s.d of values in a pixel produces an estimate of the error.

In previous studies (Van Waerbeke et al. [2013](#); Chang et al. [2018](#); Oguri et al. [2018](#)), noise maps have been generated by shuffling the galaxy shear measurements and keeping their positions constant.
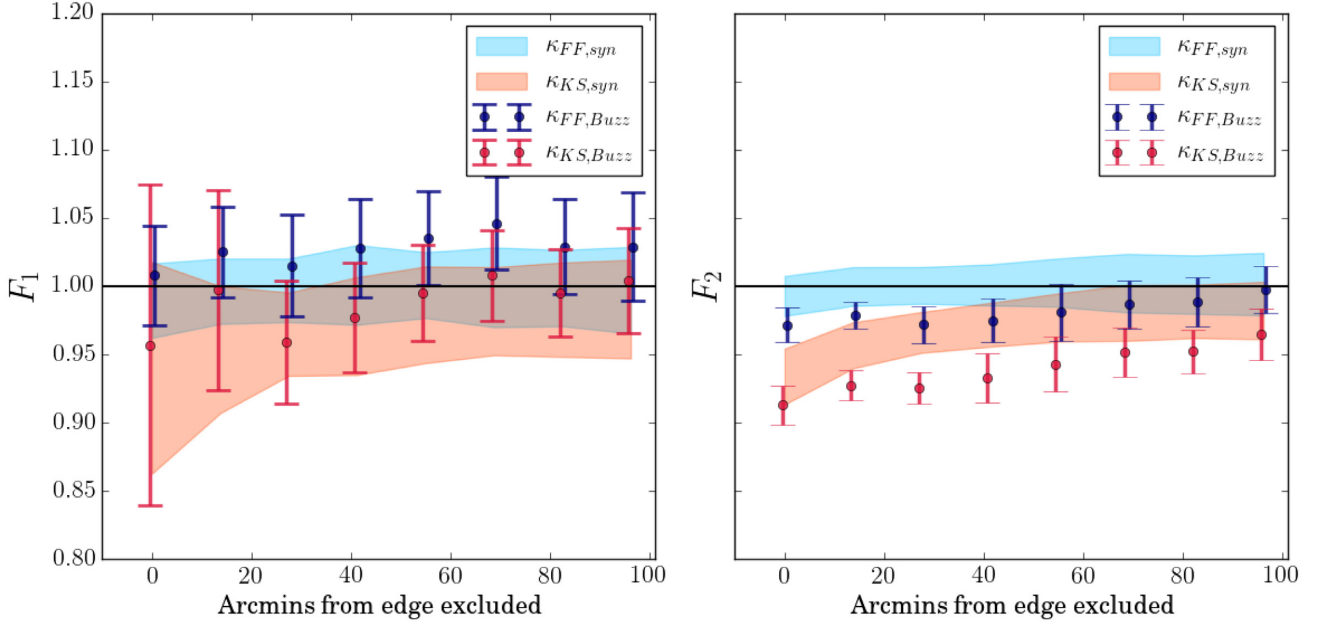
Figure 3. The *F* statistics for the two reconstruction methods in multiple simulation tests. The solid filled regions are for the Gaussian simulations with known noise properties, and the scatter points are for the Buzzard simulations. The horizontal axis represents the width of the pixel range around the edge of the surveyed area which is removed before calculating *F* for the remaining areas of the footprint. Noise estimates for the Buzzard simulations were found by using the residuals from a fitted sky and a known, Gaussian simulated truth using synfast. The F_1 statistic has been denoised, but the F_2 statistic does not require this procedure.
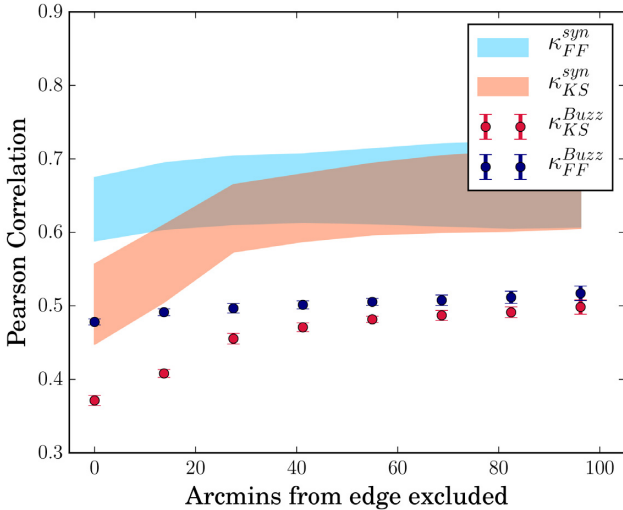
Figure 4. The Pearson correlation coefficient between the different reconstruction techniques and the true convergence κ_t, excluding pixels that fall within a given distance of the edge of the survey. The results for both the simulations using synfast (filled region) and those using the Buzzard simulation are shown. The deterioration of the reconstructions as the edge pixels are included in the measurement of the statistic can be interpreted as the contribution from these more noisy pixels reducing the correlation. Significant improvement in correlation can be seen as the noisier exterior pixels for κ_{KS} are excluded, but for κ_{FF} the variation due to excluding these pixels is much less pronounced.

This is an alternative but equivalent method to that used in this paper, as it also removes any signal present from cosmic shear and produces mass maps consisting only of noise. Both techniques model shape noise, mask effects, and variations in the galaxy number density,

and produce similar noise estimates. As our forward fitted maps require the error on a shear measurement in a pixel in order to fit to the data, we chose to use this same error field to produce our noise maps.

4.3 Galaxy survey simulations

Further to the Gaussian simulations, we also test the reconstructions using the Buzzard simulations (DeRose et al. 2019), specifically the 'Buzzard v1.3' mock galaxy catalogues. These catalogues are for six simulations resembling the DES Y1 data set, with accompanying galaxy shears, ellipticities and κ.

These were produced via N-body simulations consisting of only dark matter, in a flat ΛCDM Universe, through the use of LGADGET-2 (Springel 2005) with initial conditions from 2LPTIC (Crocce, Pueblas & Scoccimarro 2006) and using outputs from CAMB (Lewis & Bridle 2002). Three boxes sized 1050^3, 2600^3, and 4000^3 Mpc$^3 h^{-3}$ were simulated using 1400^3, 2048^3, and 2048^3 particles respectively, assuming a background cosmology of $\Omega_m = 0.286$, $\Omega_b = 0.047$, $\sigma_8 = 0.82$, $h = 0.7$, $n_s = 0.96$, and $w = -1$. The coarser simulations were used to produce sufficient volume for DES, and the higher resolution output was used to tune smaller scale modelling. It is worth noting that all of these parameters are consistent with the results found in the DES Y1 3×2-pt results (DES Collaboration 2017) even though perfect modelling of cosmological parameters is not necessary to test the mass reconstruction.

Using the outputs of these simulations, the empirical addgals algorithm (DeRose et al. 2019) populated the haloes with galaxies, replicating results found with subhalo abundance matching (SHAM) (Conroy, Wechsler & Kravtsov 2006; Reddick et al. 2013) by fitting a model to a smaller, higher resolution simulation and applying this model to the larger simulation. addgals simulta-
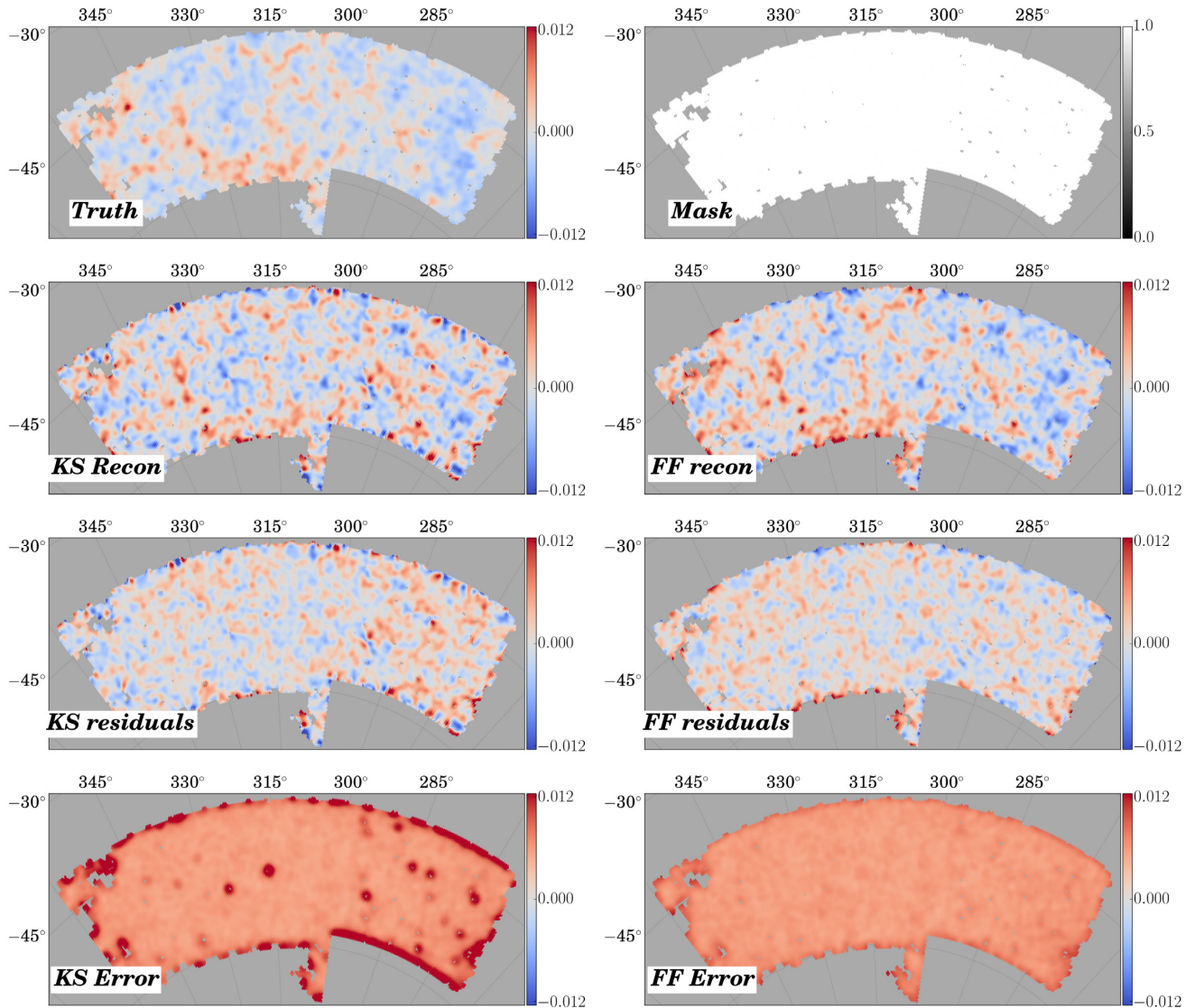
Figure 5. Reconstructions of the convergence field for the Buzzard simulation for both the direct inversion (left-hand column) and the fitting method (right-hand column). Smaller errors are present in the edge pixels of the fitted map. The fitting method also has a much more uniform residual map inside the footprint, whereas the direct inversion has a large portion of the survey with slightly larger residuals.

neously fits both the distribution of galaxy overdensities and the distribution of *r*-band absolute magnitudes of galaxies, through matching a luminosity function to observed galaxy counts. These galaxies are further provided with full SEDs from SDSS DR6 (Adelman-McCarthy et al. 2008) to produce the *grizY* magnitudes.

Lensing parameters are also computed for the catalogues, in the form of γ and κ for each galaxy. This is done through the use of the multiple plane ray-tracing algorithm Curved-sky-grAvitational Lensing for Cosmological Light conE simulatioNS (CALCLENS; Becker 2013). The routine uses projected density fields to produce weak lensing maps, with a resolution of $\simeq 6.4$ arcsec. The effects of adding photometric noise, shape noise, and imposing cuts similar to those in the data catalogue, as described in Section 5.1, are also accounted for to produce an output similar to that of DES Y1. The simulated region is smaller than the full DES Y1 observed region by ≈ 600 deg, and its galaxy density count is lower by $\simeq 20$ per cent.

We apply the forward fitting method to the Buzzard data and output a final map, which is an average of many fitted maps

consistent with the data. We estimate the pixel error distributions using further simulated SYNFAST(Górski et al. 2005) skies with the same footprint as the Buzzard map, and examine the residuals across an ensemble of final fitted maps and the true κ map in each case. These simulations serve as a simple model of the lensed Universe that we are observing: a uniform source plane of galaxies which undergo a lensing effect, on to which a shape noise component is added. In reality, the broad redshift bins that we use to produce sufficiently large galaxy counts on the source plane mean that this model is a simplification, but we will see that it provides a sufficient estimate of errors for our purposes.

The maps produced for the Buzzard simulation are shown in Fig. 5 and the residuals for the forward fitting method can be seen to be much lower in the outer edge regions, similar to that found for the Gaussian simulations, although the errors are now slightly larger. This may be due to non-Gaussianities in κ_t, or due to the extra noise inherent in all of the Buzzard simulated maps, where we do not have an exact value for the true κ and shear in a pixel but
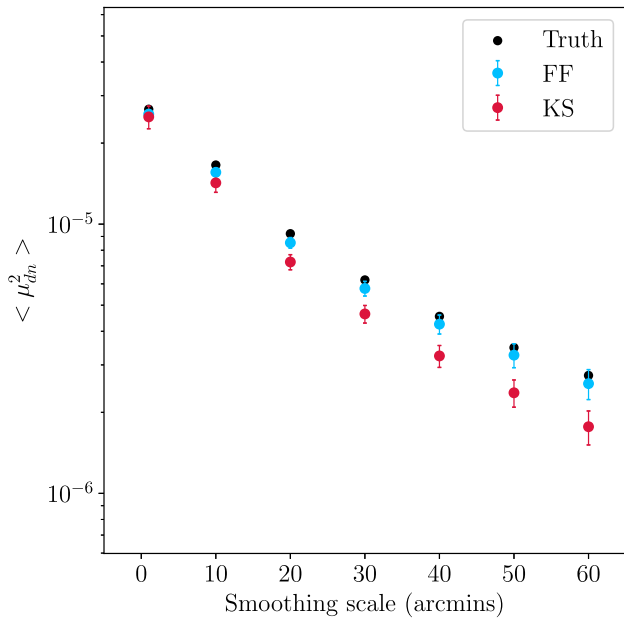
Figure 6. Reconstruction of the second moment of the κ field from equation (16) for the forward fitting and direct inversion methods, together with true values, for a Buzzard simulation.

instead estimate it from the measured quantities for galaxies within that pixel.

4.3.1 F statistics

The F statistics for Buzzard are plotted as the scatter points on Fig. 3. In the case of F_1, the denoised statistic can be seen to be consistent with that found for the Gaussian maps, meaning that our estimate of the noise for these Buzzard simulations is reliable. For F_2 both techniques appear to behave slightly worse than in the previous simulations, due to additional noise in Buzzard. The slightly lower F_2 and slightly high F_1 indicate that this map has larger residuals than that typically found for the Gaussian maps, but these are still consistent with our expectations.

4.3.2 Pearson correlation

The Pearson correlation coefficient measurements can be seen in Fig. 4 for both reconstructions and for both methods of simulating the data. The `synfast` simulations have a higher coefficient for both techniques, and each simulation shows a similar shape when comparing the same reconstruction methods. It is apparent that the statistics found for the fitted maps are significantly less affected by removing outer pixels than for the direct inversion, suggesting the presence of excess noise in the edge pixels of the direct inversion.

4.4 Moments

Summary statistics such as moments can be very useful probes to test the accuracy of our final maps. Beyond characterizing the distribution, the moments as a function of the smoothing scale have also been shown to be useful for constraining the underlying cosmology.

When measuring these moments, we are measuring a combination of the true convergence moment and a noise term. We correct

for the noise following the technique used in Van Waerbeke et al. (2013) and the methodology introduced in equation (14), such that for the second moment the denoising procedure is:

$$\langle (\mu_{dn})^2 \rangle = \langle (\mu_N)^2 \rangle - \langle (\mu_n)^2 \rangle, \tag{16}$$

where μ_n is the κ field found for the noise exclusively, μ_{dn} is the denoised κ, and μ_N is the moment found from the noisy field.

Fig. 6 shows the reconstruction of these denoised moments for both methodologies on one of the Buzzard simulations. At large smoothing scales, the edge effects from the direct inversion become more and more significant such that the moments become increasingly biased away from the truth. The forward fitting approach does not have this level of significant error localized around the edge of the map, so it can reconstruct the moment more reliably to higher smoothing scales. At higher pixel resolution, these edge effects will become less significant as edge pixels account for a smaller fraction of the total pixel count.

4.5 PDF

The PDFs of the convergence distributions serve as a further probe of the reconstruction, and these are shown in Fig. 7. The large contribution of the noise added to the data can be seen to cause the final PDF to differ significantly from the underlying, non-Gaussian true κ PDF. The PDF of our estimated noise distribution is also shown, as well as the PDF of the exact differences between the reconstructions and the truth. These estimates of the noise and the true residuals can be seen to be in good agreement, indicating a good understanding of the noise properties of both methods. Further, the PDF of the κ distribution in the forward fitting method manages to retain more of the non-Gaussian shape and does not find an excess of high κ values in edge pixels. The forward fitting method finds fewer of the large, negative convergence values which are introduced by the direct inversion but reconstructs a similar number of higher positive κ peaks to the direct inversion. Some overdense regions will be real density contrasts, for which both techniques should agree, and some will be the large edge effects that are only present in the direct inversion.

We also examine the agreement of these two distributions using the Jensen–Shannon divergence D_{JS}, a quantity designed for such a comparison in an information theory context. This is defined, for two distributions A(x) and B(x) as

$$D_{JS}(A, B) = \frac{1}{2}(D_{KL}(A||M) + D_{KL}(B||M)), \tag{17}$$

where

$$M = \frac{1}{2}(A + B), \tag{18}$$

and D_{KL} is the Kullback–Leibler divergence, defined for discrete bins as

$$D_{KL}(A||B) = \sum_x A(x) \log \frac{A(x)}{B(x)}. \tag{19}$$

We work in logarithms of base 2, which means that the Jensen–Shannon divergence can be in the range 0–1, with 0 indicating identical distributions and 1 meaning completely different distributions. This provides a way to quantify the similarity between the PDFs of each reconstruction and the known, true κ PDF. In the unsmoothed κ fields, we find that for the direct inversion $D_{JS} = 0.349$, whereas for the forward fitted map $D_{JS} = 0.308$. In the smoothed maps shown in Fig. 5, the result for the direct inversion is $D_{JS} = 0.115$, compared to $D_{JS} = 0.103$ for the forward fitted maps. These values show that
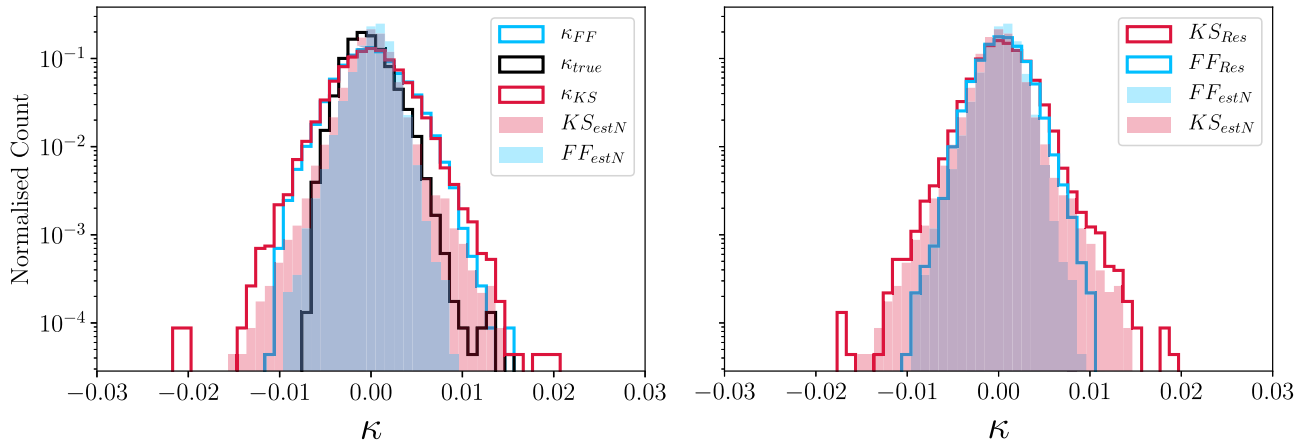
Figure 7. PDFs of the reconstruction techniques' convergence fields compared to the true distribution for the smoothed Buzzard simulation shown in Fig. 5. The left-hand panel shows the distribution of the κ in pixels (solid lines), together with the estimated noise distribution (filled region). The solid black line is the true PDF that both reconstructions are attempting to recover. The right-hand panel examines the reliability of the estimates used for the noise distribution, with solid fill areas denoting the true residuals and the solid lines denoting the noise estimates used in the left-hand panel.
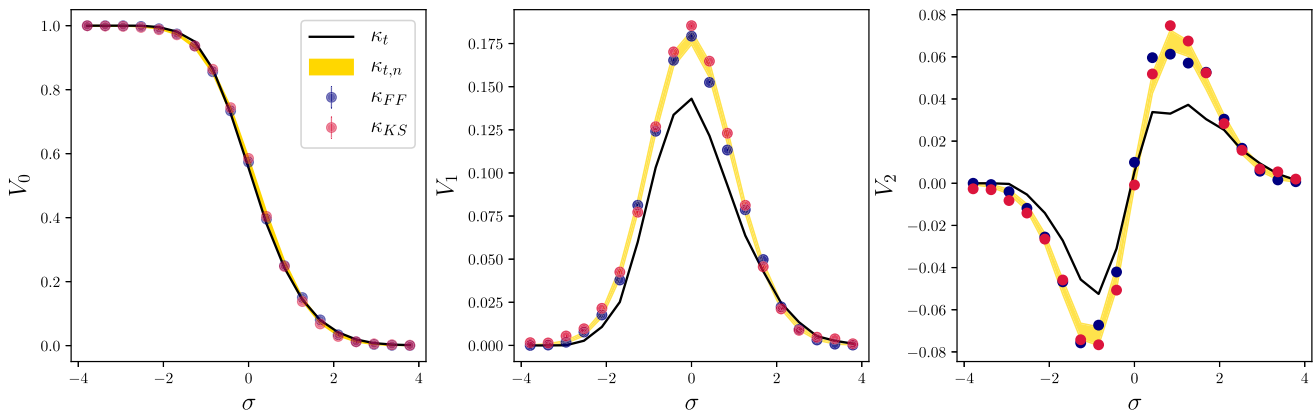
Figure 8. The Minkowski functionals for a Buzzard simulation used to test the κ map reconstructions. In this case, σ indicates the number of standard deviations of the final κ map and not the error in a pixel. The black line shows the functionals for the true κ field and the yellow field region shows the 68 per cent confidence region for functionals expected when a simple Gaussian noise field is added to this. The Minkowski functionals measure the topology of the maps and perfect agreement between truth and reconstruction across all three statistics would mean that all topological information is being retained by the reconstruction.

while both methods are finding rather similar distributions to the desired, true PDF, the forward fitted maps are performing slightly better. We can interpret this result as showing that the forward fitted map has a reduced noise component. From inspection of the PDFs, it can be seen that this is indeed the case in the tails of the distribution.

4.6 Minkowski functionals

Fig. 8 shows the Minkowski functionals reconstructed for the Buzzard simulation. The solid black line shows the functionals for the κ_t field, and the yellow region shows those that we would expect to construct for this field in the presence of noise. The deviations between the functionals for κ_t and those in the presence of noise are greatest within a few standard deviations from the mean; this standard deviation approximately coincides with the noise level of these maps. This is expected, as the noise adds artificial peaks of this amplitude which will change the functionals; reducing the noise level would make it easier to distinguish between cosmologies. Particularly in the direct inversion, the edge effects will introduce some large κ values into the distribution and this will

alter the standard deviation of the map and consequentially bias the functional measurement. This means that when we attempt to constrain cosmology with these measurements, the reconstruction technique used needs to be taken into account and adequately modelled.

We now assess the significance of the agreement between the functionals measured for the reconstructions, and the expectation from the true field with added Gaussian noise. We calculate

$$\chi^2 = (d - t)\text{Cov}^{-1}(d - t)^T, \qquad (20)$$

where d is the vector of functionals calculated for a reconstruction, t is the vector of functionals for the true κ field, and Cov is the covariance matrix calculated by examining the covariance between these functional bins when noise is added to the true κ. This noise is created by generating maps of ellipticity noise, i.e for a pixel i, noise is found by randomly sampling from a Gaussian with width according to the error on shear in that pixel. For empty regions of the sky, we fill these areas with noise with the average shear standard deviation of the observed region. These shear maps are then used to produce full sky κ maps through the direct inversion.
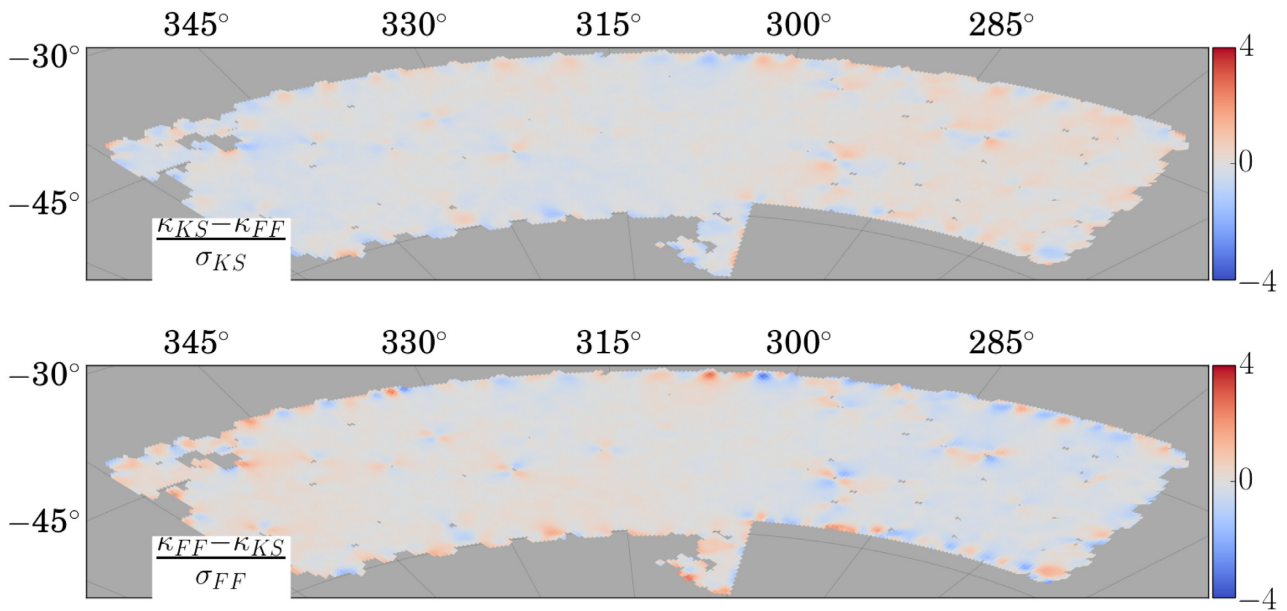
Figure 9. The difference between κ maps found for both reconstruction techniques on one of the Buzzard simulations. As each map technique has different errors in each pixel, the level of tension in terms of standard deviations in a pixel depends upon which map is used as a reference. Disagreements between the direct inversion and the forward fit around the survey edge are of larger significance in terms of σ_{FF}, indicating that the forward fit is highlighting these particular pixels in the Kaiser–Squires map as being due to edge effects and not caused by the shear signal in the observed region.

Edge effects are absent from these maps, as the γ noise fields are on the full sky, and as such provide a best case scenario for the noise on our final κ maps. We are only considering shape noise in our covariance, although we anticipate other contributions to be subdominant. Initial tests using Gaussian simulated fields supported this assumption.

For binning functionals into n bins, we produce $4n$ of these noise maps. Each noise field is then added to the true κ_t field and the functionals calculated. We use this ensemble of functionals to measure covariances between bins for our χ^2 calculation, through repeatedly producing new noisy versions of κ_t fields.

This approach gives us a way to compare both techniques' abilities to reconstruct the functionals, taking into account the level of shape noise in the data. For the Buzzard simulation results shown in Fig. 8, the reduced χ^2 results for (v_0, v_1, v_2) give (75/19, 120/19, 73/19) for the direct inversion and (48/19, 38/19, 38/19) for the forward fitting routine. This significant improvement shows the impact that edge effects can have on final results for direct inversion; accounting for this is important, as it can bias the final result.

4.7 Comparing residuals

The two reconstruction techniques produce different κ maps for the same data, so an interesting comparison is to examine the regions in which they disagree and see what can be learned in these areas. We examine the differences between two maps in ratio to the error in each map in Fig. 9. First, by visual inspection, the κ_{KS} map can be seen to be in much more significant disagreement with the κ_{FF} map when differences are taken in terms of σ_{FF} than σ_{KS}. This inconsistency is another illustration of the noise introduced by the Kaiser–Squires technique when directly applied to the data. Further to this, considering the signal to noise of these differences in each pixel can highlight tensions between the maps. The two methods are in agreement across large areas of the centre of the footprint, but the edge effects present in the direct inversion κ_{KS} map mean

that there is a tension with the forward fitted map. In the 750 pixels where there is a disagreement of $2\sigma_{FF}$ or more, the forwards fitting method has a smaller residual with κ_t than the direct inversion in 81 per cent of pixels.

5 DES Y1 RESULTS

Following the successful reconstructions of the convergence maps on simulations, we apply the technique to real data from the DES (Flaugher 2005).

5.1 Data

The DES is a photometric survey using the Dark Energy Camera (Flaugher et al. 2015) on the Blanco telescope, a 4 m telescope at the Cerro Tololo Inter-American Observatory in Chile. Observations are taken in five bands (*grizY*). This work makes use of the data from the first full year of observations, also known as the DES Y1 cosmology data set, or Y1A1 GOLD (Drlica-Wagner et al. 2018). This footprint is the one best suited to the application of the mass mapping techniques to date, as it spans a substantial survey area of $\approx 1800\,\mathrm{deg}^2$ and contains sources up to a redshift of $\simeq 1.3$.

5.2 Weak lensing catalogues

We use the METACALIBRATION catalogue, which is described in Huff & Mandelbaum (2018) and Sheldon & Huff (2017). This method for calibrating lensing measurements uses the data itself, as opposed to simulations of galaxies, by applying a known shear to deconvolved galaxy images. These galaxy shapes are measured using a Gaussian profile, fit with NGMIX (Sheldon 2015) and a comparison between the measurement of the change in galaxy shape and the known applied shear gives the *response*. There are three biases associated with this technique: a multiplicative bias m, an additive bias α from the PSF ellipticity, and an additive bias β from
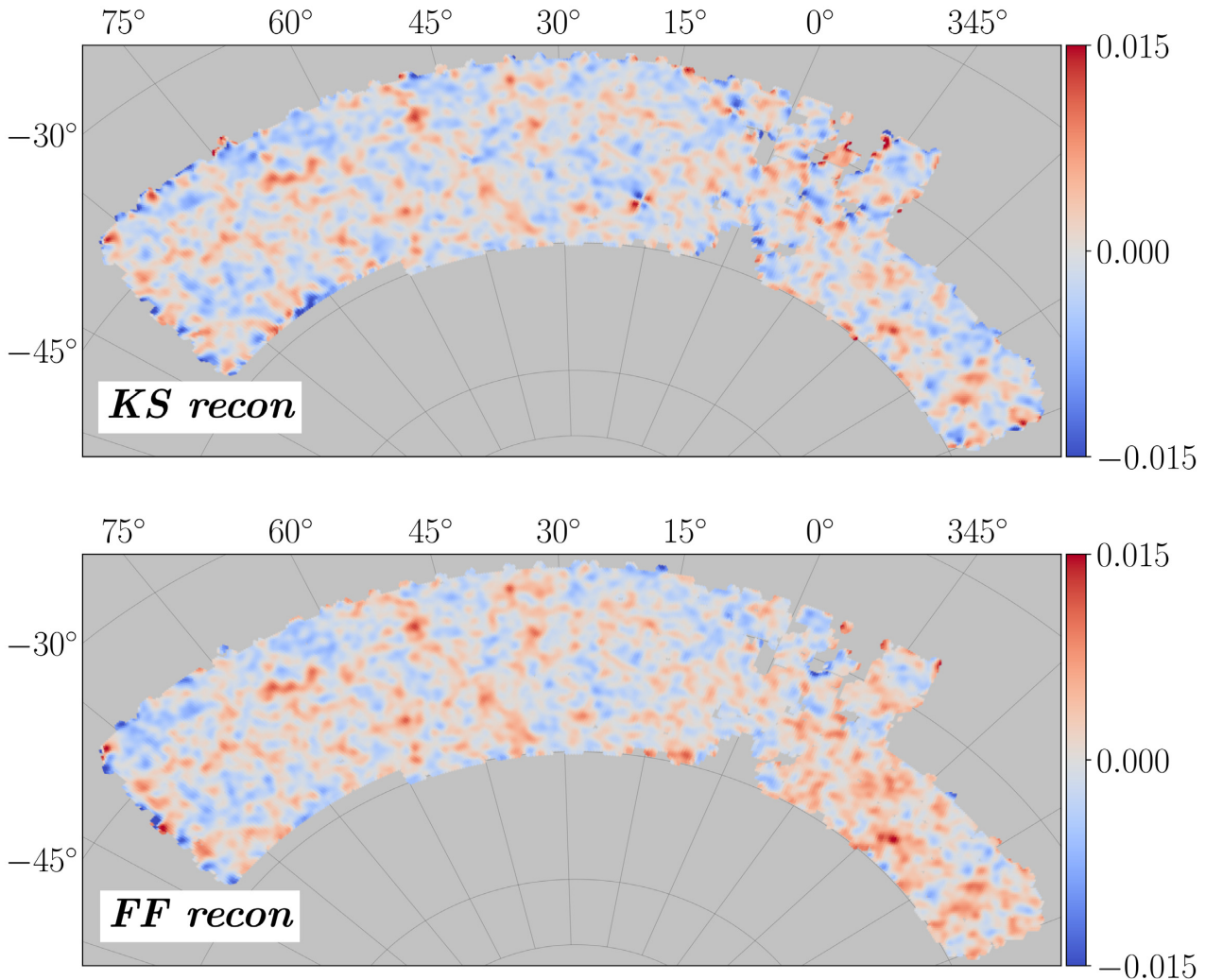
Figure 10. The final fitted maps for the DES Y1 data for both the direct inversion and the forward fitting method, using `nside = 256`. The area of complicated masking on the right-hand side of the mask, at greater than 300 deg and less than < 5 deg on the Figure, was not used in our previous wide-field mass map paper due to the footprint introducing significant edge effects. Despite this, a large quadrupole pattern is still present in an inner region of the mask due to a small area of missing shear data. This is more visible in this analysis that previous higher *nside* maps due to the larger contribution of edge effects.

the error on the PSF ellipticity. Zuntz et al. (2018) found these to be $m = 1.2 \pm 1.3$ per cent, $\alpha \approx 0$ and $\beta \approx -1$. `metacalibration` in DES uses images from r, i, and z bands and the code is available publicly with the `ngmix` routines.[4]

The DES also used the IM3SHAPE routine for producing the weak lensing catalogues and both catalogues were examined in Zuntz et al. (2018). The κ maps produced from both catalogues were compared in Chang et al. (2018) and found to be consistent with each other. We choose to produce maps solely on the METACALIBRATION catalogue, as this has reduced systematics and a larger galaxy count; there are $\approx 34\,800\,000$ galaxies in the METACALIBRATION catalogue, compared to $\approx 21\,900\,000$ in IM3SHAPE, due to the latter only fitting objects in the r band.

5.3 Redshift binning

Redshift information in the DES Y1 data catalogue is found by implementing a Bayesian Photometric Redshift (BPZ) algorithm

as used in Benítez (2000) and Coe et al. (2006), making use of galaxy templates from Bruzual & Charlot (2003), Kinney et al. (1996), Coleman, Wu & Weedman (1980) to produce a posterior distribution of the redshift of the observed galaxy. We use the mean of this distribution in selecting the galaxies in a redshift range of 0.3 to 1.2, which are chosen as our source galaxies. We use the redshifts calculated using the METACALIBRATION photometry. The full routine is described in Hoyle et al. (2018), and the use of cross-correlation redshifts was tested in Gatti et al. (2018) and Davis et al. (2017). REDMAGIC (Rozo et al. 2016) galaxies were used as a reference sample for the redshifts, which were in turn calibrated through comparison with BOSS galaxies (Cawthon et al. 2018).

5.4 The DES Y1 fitted maps

The fitted maps for the DES Y1 data are shown in Fig. 10 for the forwards fitting and the Kaiser–Squires methods, applied to the full area of the `metacalibration` catalogue. The maps presented here are for the redshift range $0.2 < z < 1.3$, for the highest density of source galaxy shapes, to reduce shape noise to
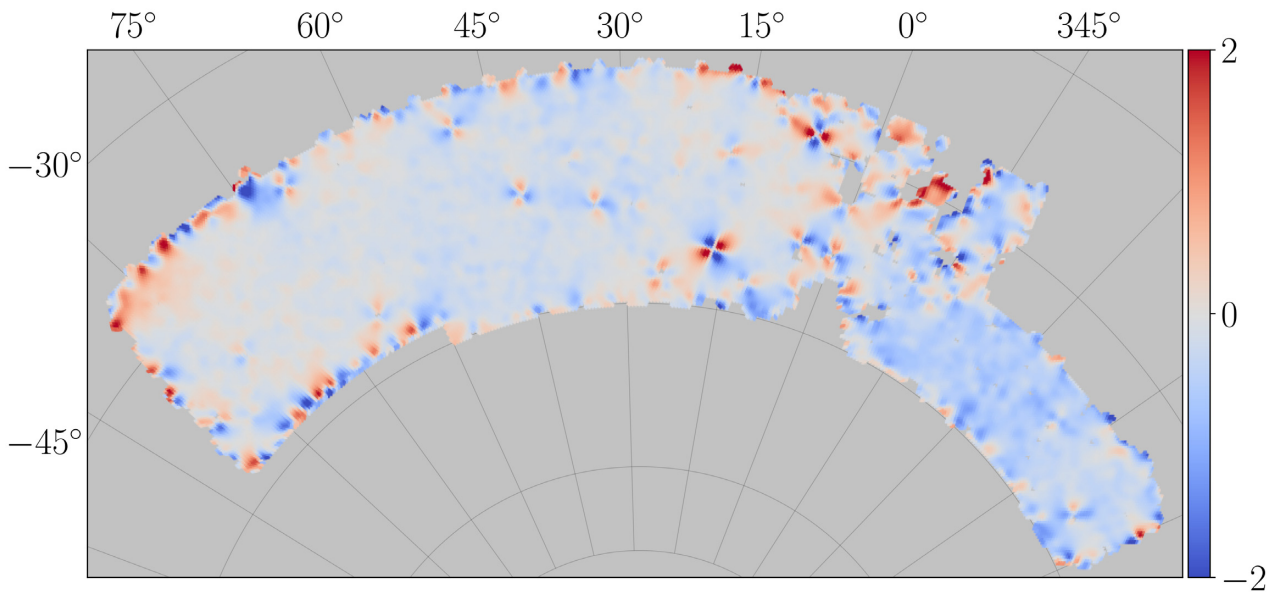
Figure 11. The residuals between the two reconstruction techniques, scaled in terms of the error on the forward fitting method in each pixel, and smoothed with a Gaussian of $\sigma = 20$ arcmin. As expected, the most significant differences arise in the areas around the edges and in areas of complicated masking.
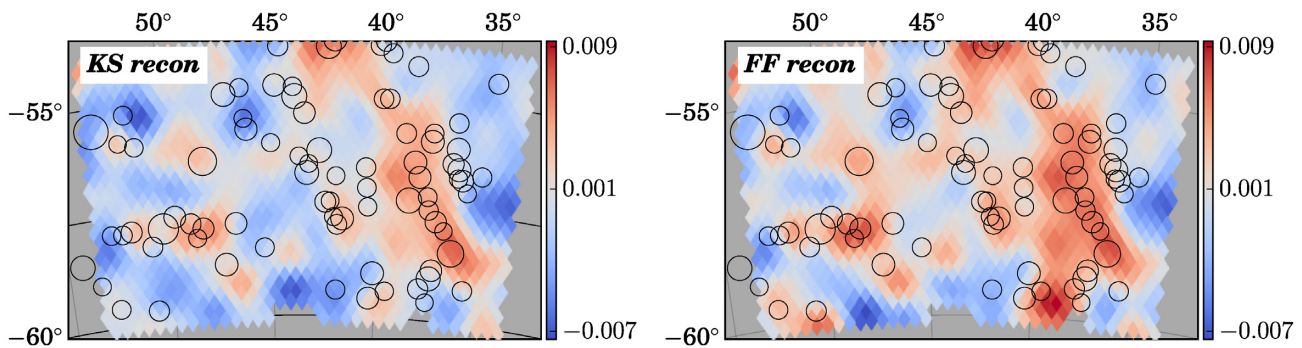
Figure 12. A section of the reconstructed maps, with REDMAPPER clusters plotted in black circles, with a radius scaling as the cluster richness λ. λ is an estimate of the number of red-sequence cluster member galaxies and is an indicator of cluster mass. Larger circles indicate clusters with higher richnesses. Clusters were selected in the redshift range $0.1 < z < 0.4$, and only clusters with a richness greater than 25 are included in this plot.

a minimum (Chang et al. 2018). These maps are visually very similar in the inner regions of the map, where peaks in one map frequently coincide with peaks in the other map. The edge effects are apparent in the reconstruction of the direct inversion in the area of complicated masking (below 5 deg in right ascension) whereas such high κ pixels are not produced in the fitted version of the map. This behaviour is similar to that seen in the previous simulations in Section 4.

Fig. 11 shows residuals between the reconstructions. The direct inversion performs well for κ reconstructions well inside the survey footprint, and we see that both methods are working in a similar way in this area as they were in the simulations. In the outer pixels, the differences are typical of those that we would expect from the edge effects, where large κ noises and biases are introduced. The smaller errors of the fitting routine in these edge pixels means that these noisy pixels in the direct inversion are in tension with the fitted results. In more complicated regions of the mask, there are more frequent disagreements between the two methods, and our tests in Section 4 imply that the forwards fitting method is more suited to these areas.

Fig. 12 shows an area of both reconstructed fields with REDMAPPER clusters (Rykoff et al. 2016) plotted on top. This region is on the southern edge of the survey area. Both maps produce fields of similar morphology, but the forward fitted map has higher peaks due to lacking the edge biases introduced by the direct inversion. Some clusters follow the structure picked out by the maps, with areas of overdensity being more frequently populated by clusters.

5.5 Systematics

It is important to correlate these maps with other quantities that are expected to be uncorrelated with the shear in a pixel, to test whether our measurements are free from systematic effects. A significant correlation between our maps and another quantity would indicate how we are not solely inferring mass associated with weak lensing shear, but have a signal contaminated by another source.

We will examine the correlation between the observed shear measurements and other observed quantities which could plausibly cause systematic effects, such as the PSF, the airmass, the sky noise and background, across the *griz* filters. Using maps M^s of these
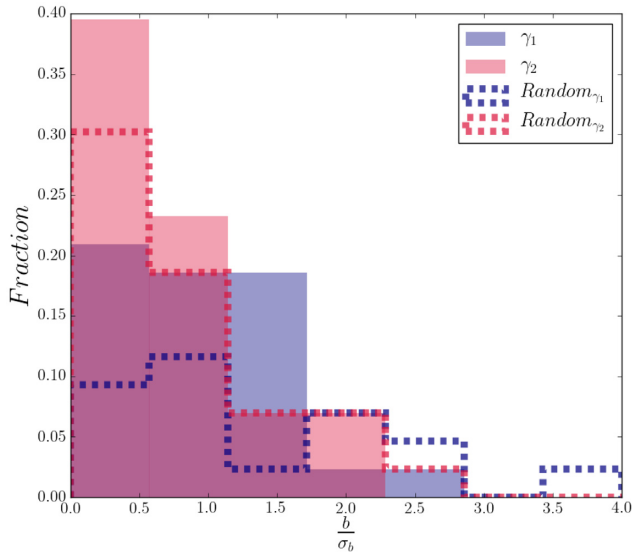
Figure 13. The distribution of the magnitude of systematics correlations found for both the Y1 data and for random maps generated using the Buzzard simulations. The latter give an indication of the level of correlation that can arise from random, uncorrelated maps, and therefore give an estimate of an acceptable level of correlation to be found with the Y1 maps.

observed parameters (Leistedt et al. 2016), we follow the approach used in Chang et al. (2018). Each pixel in the map is assigned a value n between 1 and 10, determined by which decile in the range for that systematic that it belongs to. We then take the average shear value of all pixels of a given n, $\hat{\gamma}_n$. A first degree polynomial is fitted between n and $\hat{\gamma}_n$, with y intercept a and gradient b. The gradient found in this way will therefore indicate a correlation between the shear estimate and the systematic, and a lack of correlation will be indicated by a gradient consistent with 0. Errors on the gradient are found by jackknife resampling.

Fig. 13 shows the extent of these correlations found for the Y1 data; we see that the correlation between the Y1 data and systematics is no stronger than that found between the systematics maps and a completely uncorrelated map (the Buzzard map). Comparison with the level of correlation found with the Buzzard map serves to show the expected level of spurious correlation that can arise.
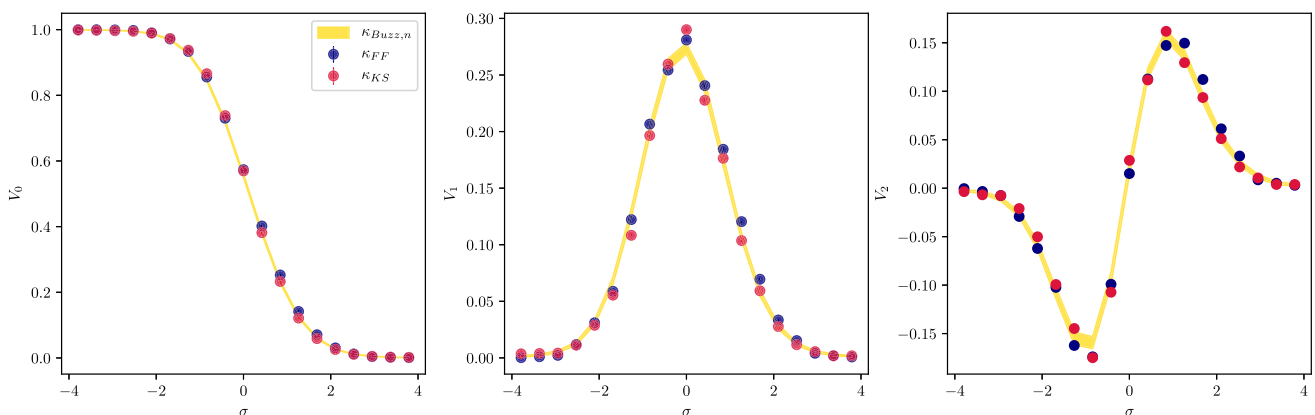
5.6 DES Y1 Minkowski functionals

Following the examination of whether the two reconstruction methods can produce reliable Minkowski functionals in Section 4, we can also examine the functionals that describe our final Y1 mass maps. We measure V_0, V_1, and V_2 (using the methodology in Appendix B) for the final Y1 convergence maps shown in Fig. 10. We present these measurements in Fig. 14, also showing the measurements and uncertainties found for these quantities in the Buzzard simulation.

As we are only comparing one particular realization of the Buzzard simulations with the Y1 results, we cannot infer cosmological information from this plot, as we do not know how representative the (finite footprint) Buzzard measurements are of the functionals expected for the Buzzard cosmology, or indeed of the real Universe. However, we see that observed Y1 Minkowski functionals appear similar to those in Buzzard. We will engage in a cosmological analysis of these results in a further paper, where noise will require careful treatment depending on the method used (i.e. direct inversion or fitting), as shown in our earlier analysis in Section 4.6.

6 CONCLUSION

Weak lensing is one of the leading probes in cosmology. Using lensing measurements across large fractions of the sky, it is possible to map the matter distribution on increasingly large scales. We have presented an alternative approach to using the Kaiser–Squires formalism to produce wide-field mass maps with weak lensing, through producing hypothesis all-sky shear fields which we fit to the data, aggregating over compatible maps.

We have tested the forwards fitting approach with simulations, and have found that in each case the resulting maps have reduced residuals compared to the direct inversion method, as well as exhibiting better agreement for the second moment as a function of smoothing scale. We have also quantified how well the methods reconstruct the topology of the maps through the use of Minkowski functionals, and found that the noise properties of the forward fitted maps avoid introducing a bias present in the direct inversion which would influence the inference of cosmological constraints.

Our approach has been applied to the DES Year 1 data and compared to the maps produced through direct inversion. This comparison finds broad agreement in central regions of the footprint, but disagreement at its edges. Our simulation tests indicate that

Figure 14. The Minkowski functionals for DES Y1 mass maps, found through both the direct inversion and the forward fitting approach. The solid yellow region shows the expected functionals for a Buzzard field with DES Y1-like noise.

these differences are symptomatic of errors introduced in the direct inversion at map edges, and that these areas of the sky are more reliably reconstructed in the forward fitted map. Our method provides a new opportunity to produce larger weak lensing mass maps to higher accuracy. Further work using this approach is worth pursuing, including producing maps to a higher resolution, use of priors on the fits, and comparison of cosmological constraints found using both the direct inversion and the fitted maps.

REFERENCES

Adelman-McCarthy J. K. et al., 2008, ApJS, 175, 297
Aihara H. et al., 2018a, PASJ, 70, S8
Aihara H. et al., 2018b, PASJ, 70, S4
Alsing J., Heavens A., Jaffe A. H., 2017, MNRAS, 466, 3272
Bartelmann M., Schneider P., 2001, Phys. Rep., 340, 291
Becker M. R., 2013, MNRAS, 435, 115
Benítez N., 2000, ApJ, 536, 571
Bruzual G., Charlot S., 2003, MNRAS, 344, 1000
Castro P. G., Heavens A. F., Kitching T. D., 2005, Phys. Rev. D, 72, 023516
Cawthon R. et al., 2018, MNRAS, 481, 2427
Chang C. et al., 2016, MNRAS, 459, 3203
Chang C. et al., 2018, MNRAS, 475, 3165
Clerkin L., Kirk D., Lahav O., Abdalla F. B., Gaztañaga E., 2015, MNRAS, 448, 1389
Coe D., Benítez N., Sánchez S. F., Jee M., Bouwens R., Ford H., 2006, AJ, 132, 926
Coleman G. D., Wu C.-C., Weedman D. W., 1980, ApJS, 43, 393
Conroy C., Wechsler R. H., Kravtsov A. V., 2006, ApJ, 647, 201
Crocce M., Pueblas S., Scoccimarro R., 2006, MNRAS, 373, 369
Davis C. et al., 2017, MNRAS, preprint (arXiv:1710.02517)
de Jong J. T. A. et al., 2015, A&A, 582, A62
DeRose J. et al., 2019, preprint (arXiv:1901.02401)
DES Collaboration, 2017, preprint (arXiv:1708.01530)
Dietrich J. P., Hartlap J., 2010, MNRAS, 402, 1049
Dodelson S., Zhang P., 2005, Phys. Rev. D, 72, 083001
Drlica-Wagner A. et al., 2018, ApJS, 235, 33
Erben T. et al., 2013, MNRAS, 433, 2545
Flaugher B., 2005, Int. J. Mod. Phys. A, 20, 3121
Flaugher B. et al., 2015, AJ, 150, 150
Gatti M. et al., 2018, MNRAS, 477, 1664
Górski K. M., Hivon E., Banday A. J., Wandelt B. D., Hansen F. K., Reinecke M., Bartelmann M., 2005, ApJ, 622, 759
Hastings W. K., 1970, Biometrika, 57, 97
Heavens A., 2003, MNRAS, 343, 1327
Hikage C., Komatsu E., Matsubara T., 2006, ApJ, 653, 11
Hoyle B. et al., 2018, 478, 592
Huff E., Mandelbaum R., 2017, preprint (arXiv:1702.02600)
Hunter J. D., 2007, Comput. Sci. Eng., 9, 90
Jeffrey N. et al., 2018, MNRAS, 479, 2871
Kacprzak T. et al., 2016, MNRAS, 463, 3653
Kaiser N., Squires G., 1993, ApJ, 404, 441
Kerscher M., Schmalzing J., Buchert T., 1996, in Coles P., Martinez V., Pons-Borderia M.-J., eds, ASP Conf. Ser. Vol. 94, Mapping, Measuring, and Modelling the Universe. Astron. Soc. Pac., San Francisco, p. 247

Kinney A. L., Calzetti D., Bohlin R. C., McQuade K., Storchi-Bergmann T., Schmitt H. R., 1996, ApJ, 467, 38

Kitching T. D. et al., 2014, MNRAS, 442, 1326

Kratochvil J. M., Haiman Z., May M., 2010, Phys. Rev. D, 81, 043519

Leistedt B. et al., 2016, ApJS, 226, 24

Leistedt B., McEwen J. D., Büttner M., Peiris H. V., 2017, MNRAS, 466, 3728

Lewis A., Bridle S., 2002, Phys. Rev. D, 66, 103511

Mandelbaum R. et al., 2018, PASJ, 70, S25

Massey R. et al., 2007, Nature, 445, 286

Mecke K. R., Buchert T., Wagner H., 1994, A&A, 288, 697

Metropolis N., Rosenbluth A. W., Rosenbluth M. N., Teller A. H., Teller E., 1953, J. Chem. Phys., 21, 1087

Miyazaki S. et al., 2018, PASJ, 70, S27

Munshi D., van Waerbeke L., Smidt J., Coles P., 2012, MNRAS, 419, 536

Oguri M. et al., 2018, PASJ, 70, S26

Patton K., Blazek J., Honscheid K., Huff E., Melchior P., Ross A. J., Suchyta E., 2017, MNRAS, 472, 439

Petri A., Haiman Z., Hui L., May M., Kratochvil J. M., 2013, Phys. Rev. D, 88, 123002

Petri A., Liu J., Haiman Z., May M., Hui L., Kratochvil J. M., 2015, Phys. Rev. D, 91, 103511

Reddick R. M., Wechsler R. H., Tinker J. L., Behroozi P. S., 2013, ApJ, 771, 30

Rozo E. et al., 2016, MNRAS, 461, 1431

Rykoff E. S. et al., 2016, ApJS, 224, 1

Schmalzing J., Górski K. M., 1997, MNRAS, 297, 355

Schmalzing J., Kerscher M., Buchert T., 1996, in Bonometto S., Primack J. R., Provenzale A., eds, Dark Matter in the Universe. IOP Press, Amsterdam, p. 281

Seitz C., Schneider P., 1995, A&A, 297, 287

Seitz S., Schneider P., 2001, A&A, 374, 740

Sheldon E., 2015, NGMIX: Gaussian mixture models for 2D images, Astrophysics Source Code Library, record ascl:1508.008

Sheldon E. S., Huff E. M., 2017, ApJ, 841, 24

Springel V., 2005, MNRAS, 364, 1105

Utsumi Y. et al., 2016, ApJ, 833, 156

Van Waerbeke L. et al., 2013, MNRAS, 433, 3373

Vikram V. et al., 2015, Phys. Rev., D92, 022006

Yang X., Kratochvil J. M., Wang S., Lim E. A., Haiman Z., May M., 2011, Phys. Rev. D, 84, 043529

Zuntz J. et al., 2015, Astron. Comput., 12, 45

Zuntz J. et al., 2018, MNRAS, 481, 1149

APPENDIX A: NOISE MODELLING

Accurate quantification of the uncertainties for pixels in the fitted convergence maps is integral to understanding their reliability.
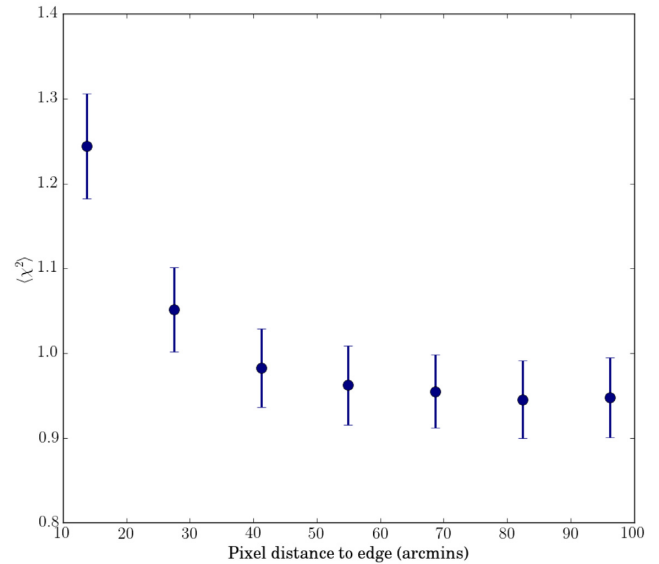

Figure A1. The average χ^2 for a set of pixels, as a function of the distance of these pixels to the edge of the fitted region, is shown for an ensemble of fits. This highlights how the routine preferentially constrains γ values in the centre of the map at the expense of producing worse γ estimates in the outer areas of the map. The overall fit to all pixels has $\chi^2/n = 1$, but as can be seen this does not force the variance for an outer pixel to be the same as that in the central region of the map.

A final fitted map is produced through averaging 40 maps resulting from our method pipeline. However, the error on the claimed convergence in each pixel of this final map is difficult to quantify. It might be thought that this could be well estimated from the standard deviation of the convergence across these 40 fits in a given pixel, but this is found, for edge pixels, to be much larger than the typical residuals between the final map and the true convergence. This can be understood by noting that a good overall fit to the data can be obtained even if the relatively small number of edge pixel values are a poorer fit. Fig. A1 shows how the mean χ^2 of the fitted shear changes as a function of the distance from the edge of the map; edge pixels are consistently further from $\chi^2/n_{\mathrm{pix}} = 1$ in all of our fitted maps. This produces a larger spread of realizations of κ in these pixels, and its standard deviation therefore has a larger range than the residuals between mean maps and the truth, as shown in Fig. A2.
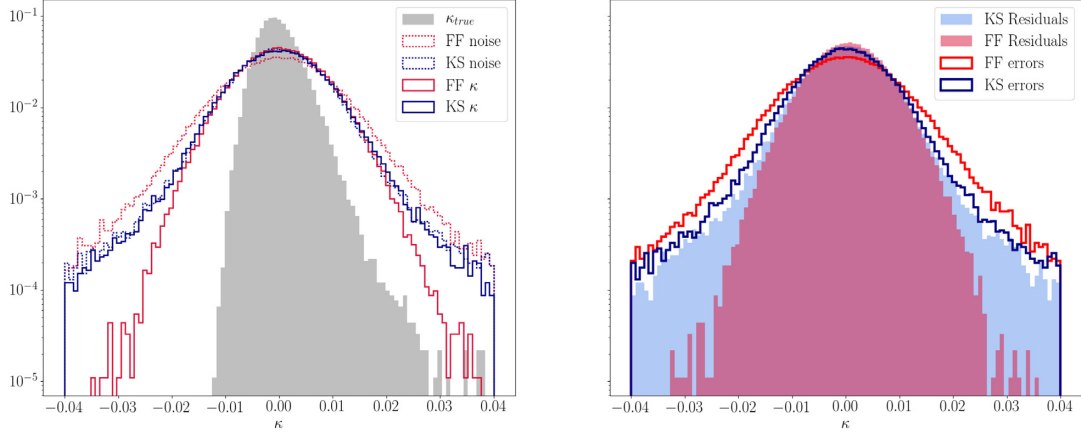
Figure A2. Left-hand panel: Distribution of convergence and associated noise for the Buzzard simulation and reconstruction. The solid lines represent reconstructed κ distributions for Buzzard. The dashed lines show expected noise, if we estimate error in each pixel from the standard deviation of κ values in an ensemble of reconstructions. Note that the dashed estimated noise distributions appear much wider than the solid reconstructed distributions (see the text for explanation). Right-hand panel: Distribution of noise estimated in two ways. The solid lines show the estimate from s.d. on κ from an ensemble of reconstructions. The filled regions show residuals directly measured between our mean reconstruction and the true convergence field.

APPENDIX B: CALCULATION OF MINKOWSKI FUNCTIONALS

We follow the approach used in Hikage et al. (2006) Appendix A to measure the Minkowski Functionals on the sphere. This approach considers the curvature of the sky and a pixelized surface. The three functionals for an excursion of size ν in a field u normalized by its standard deviation, are described by

$$V_0 = \mathcal{H}(u - \nu), \tag{B1}$$

$$V_1 = \frac{1}{4} F(u - \nu) \sqrt{u_{;\theta}^2 + u_{;\phi}^2}, \tag{B2}$$

$$V_2 = \frac{1}{2\pi} F(u - \nu) \frac{2 u_{;\theta} u_{;\phi} u_{;\theta\phi} - u_{;\theta}^2 u_{;\phi\phi} - u_{;\phi}^2 u_{;\theta\theta}}{u_{;\theta}^2 + u_{;\phi}^2}. \tag{B3}$$

The coordinates θ, ϕ refer to angular positions on the sky and a semicolon denotes a partial derivative. We use this formalism in a `python` code to calculate the functionals from HEALPIX maps.

[1]*Institute of Cosmology and Gravitation, University of Portsmouth, Portsmouth PO1 3FX, UK*
[2]*Department of Astronomy and Astrophysics, University of Chicago, Chicago, IL 60637, USA*
[3]*Kavli Institute for Cosmological Physics, University of Chicago, Chicago, IL 60637, USA*
[4]*Department of Astrophysical Sciences, Princeton University, Peyton Hall, Princeton, NJ 08544, USA*
[5]*Department of Physics, University of Arizona, Tucson, AZ 85721, USA*
[6]*Max Planck Institute for Extraterrestrial Physics, Giessenbachstrasse, D-85748 Garching, Germany*
[7]*Universitäts-Sternwarte, Fakultät für Physik, Ludwig-Maximilians Universität München, Scheinerstr. 1, D-81679 München, Germany*
[8]*Department of Physics and Astronomy, University College London, Gower Street, London WC1E 6BT, UK*
[9]*Institut de Física d'Altes Energies (IFAE), The Barcelona Institute of Science and Technology, Campus UAB, E-08193 Bellaterra (Barcelona), Spain*
[10]*Institut d'Estudis Espacials de Catalunya (IEEC), E-08034 Barcelona, Spain*
[11]*Institute of Space Sciences (ICE, CSIC), Campus UAB, Carrer de Can Magrans, s/n, E-08193 Barcelona, Spain*
[12]*Department of Physics, Stanford University, 382 Via Pueblo Mall, Stanford, CA 94305, USA*
[13]*Kavli Institute for Particle Astrophysics and Cosmology, PO Box 2450, Stanford University, Stanford, CA 94305, USA*
[14]*SLAC National Accelerator Laboratory, Menlo Park, CA 94025, USA*
[15]*Department of Physics, ETH Zurich, Wolfgang-Pauli-Strasse 16, CH-8093 Zurich, Switzerland*
[16]*Department of Physics, Carnegie Mellon University, Pittsburgh, PA 15312, USA*
[17]*Brookhaven National Laboratory, Bldg 510, Upton, NY 11973, USA*
[18]*Department of Physics, Duke University Durham, NC 27708, USA*
[19]*Institute for Astronomy, University of Edinburgh, Edinburgh EH9 3HJ, UK*
[20]*Cerro Tololo Inter-American Observatory, National Optical Astronomy Observatory, Casilla 603, La Serena, Chile*
[21]*Fermi National Accelerator Laboratory, PO Box 500, Batavia, IL 60510, USA*
[22]*CNRS, UMR 7095, Institut d'Astrophysique de Paris, F-75014 Paris, France*
[23]*Sorbonne Universités, UPMC Univ Paris 06, UMR 7095, Institut d'Astrophysique de Paris, F-75014 Paris, France*
[24]*Jodrell Bank Center for Astrophysics, School of Physics and Astronomy, University of Manchester, Oxford Road, Manchester M13 9PL, UK*
[25]*Centro de Investigaciones Energéticas, Medioambientales y Tecnológicas (CIEMAT), E-28040 Madrid, Spain*
[26]*Laboratório Interinstitucional de e-Astronomia - LIneA, Rua Gal. José Cristino 77, Rio de Janeiro RJ - 20921-400, Brazil*
[27]*Department of Astronomy, University of Illinois at Urbana-Champaign, 1002 W. Green Street, Urbana, IL 61801, USA*
[28]*National Center for Supercomputing Applications, 1205 West Clark St., Urbana, IL 61801, USA*
[29]*Observatório Nacional, Rua Gal. José Cristino 77, Rio de Janeiro, RJ - 20921-400, Brazil*
[30]*Department of Physics, IIT Hyderabad, Kandi, Telangana 502285, India*
[31]*Department of Astronomy, University of Michigan, Ann Arbor, MI 48109, USA*
[32]*Department of Physics, University of Michigan, Ann Arbor, MI 48109, USA*
[33]*Instituto de Fisica Teorica UAM/CSIC, Universidad Autonoma de Madrid, E-28049 Madrid, Spain*

[34] *Santa Cruz Institute for Particle Physics, Santa Cruz, CA 95064, USA*

[35] *Center for Cosmology and Astro-Particle Physics, The Ohio State University, Columbus, OH 43210, USA*

[36] *Department of Physics, The Ohio State University, Columbus, OH 43210, USA*

[37] *Center for Astrophysics, Harvard and Smithsonian, 60 Garden Street, Cambridge, MA 02138, USA*

[38] *Department of Physics and Astronomy, University of Pennsylvania, Philadelphia, PA 19104, USA*

[39] *Australian Astronomical Optics, Macquarie University, North Ryde, NSW 2113, Australia*

[40] *Departamento de Física Matemática, Instituto de Física, Universidade de São Paulo, CP 66318, São Paulo, SP 05314-970, Brazil*

[41] *George P. and Cynthia Woods Mitchell Institute for Fundamental Physics and Astronomy, and Department of Physics and Astronomy, Texas A&M University, College Station, TX 77843, USA*

[42] *Institució Catalana de Recerca i Estudis Avançats, E-08010 Barcelona, Spain*

[43] *School of Physics and Astronomy, University of Southampton, Southampton SO17 1BJ, UK*

[44] *Instituto de Física Gleb Wataghin, Universidade Estadual de Campinas, 13083-859 Campinas, SP, Brazil*

[45] *Computer Science and Mathematics Division, Oak Ridge National Laboratory, Oak Ridge, TN 37831, USA*

[46] *Argonne National Laboratory, 9700 South Cass Avenue, Lemont, IL 60439, USA*

This paper has been typeset from a TeX/LaTeX file prepared by the author.